International Journal for Housing Science and Its Applications
Publish August 10, 2025. Volume 46, Issue 4 Pages 7712-7727

https://doi.org/10.70517/ijhsa464664

Multi-dimensional filtering and intelligent extraction algorithm for structural parameters of cable point cloud images

Zihan Dong[1,*], Wenchao Ding[1], Hong Wang[2], Wangqiang Wu[1], Lei Lei[2,3] and Liang Wang[2,3]
[1] State Grid Weinan Power Supply Company, Weinan, Shaanxi, 714000, China
[2] State Grid (Xi'an) Environmental Technology Center Co., Ltd., Xi'an, Shaanxi, 710000, China
[3] Electric Power Research Institute of State Grid Shaanxi Electric Power Co., Ltd., Xi'an, Shaanxi, 710000, China

Corresponding authors: (e-mail: zihandongys@sina.com).

Abstract This study first introduces the basic principles of laser triangulation and the principles of handheld laser scanners, and then applies point cloud reduction and point cloud smoothing methods for data processing. Addressing the issue that conventional point cloud filtering methods can cause data degradation in noisy environments, this study proposes a point cloud filtering algorithm that combines dual tensor voting and multi-scale normal vector estimation. By comparing different filtering algorithms and conducting visual analysis across various scenarios, the proposed method is evaluated. Additionally, the Q3D software is used to establish a cable layout model and perform simulation calculations. Experimental results show that the improved algorithm demonstrates good robustness in different scenarios, effectively enhancing noise removal rates while minimizing the loss of environmental features, and maintaining good algorithmic efficiency. Additionally, simulation results indicate that the improved method can quickly and conveniently extract cable distribution parameters. Finally, by applying the proposed method, an improved cable design scheme is proposed, and it is found that the average stranding pitch of the improved power cables is 167, within the standard range.

Index Terms point cloud filtering, multi-scale normal vector estimation, parameter extraction, cable

I. Introduction

The energy industry is a foundational sector critical to national economic development and public welfare. Since the implementation of reform and opening-up, China's economic construction has achieved remarkable accomplishments, and the sustained, healthy, and efficient development of the power industry has been an indispensable factor in this progress. As China's urbanization process accelerates and power demand continues to grow, the quality of cable accessory installation directly impacts the safe operation of power cables, and non-compliant installation can lead to insulation failures in power cables [1], [2]. Concurrently conducting third-party quality inspections during installation is an important task for grid operation and maintenance departments within the power system [3]. Due to complex terrain and climate conditions, as well as the limitations of manual inspection methods, traditional power line inspections are labor-intensive, inefficient, inaccurate, and prone to missed inspections, making them increasingly unsuitable for the growing scale and efficiency requirements of modern power grids [4]-[7]. With advancements in technology and improvements in economic levels, manned and unmanned helicopters equipped with sensors have gradually been applied to transmission line inspections, effectively enhancing the efficiency of transmission line inspection tasks [8]-[10]. These technologies primarily detect faults through image processing, enabling automatic or manual interaction to identify issues such as overheating and arcing in transmission lines [11], [12].

Research on power equipment monitoring technology using two-dimensional images has already reached a high level of maturity [13]. With the advancement of artificial intelligence, 3D point clouds, which possess the advantage of a third spatial dimension, can maximally restore the original shape information of power equipment, making them a future research trend and focus in the field of machine vision within the power industry [14]-[16]. Cables, as the primary medium for transmitting electrical energy, are the foundation for ensuring the normal and stable operation of power equipment [17]. 3D point cloud cable data directly obtained through 3D scanning devices contains various types of noise, which affects the overall quality of the point cloud, misleads the estimation of local point cloud features, and not only impacts visual perception but also poses challenges for 3D point cloud cable segmentation and identification [18]-[21]. To reduce the estimation errors caused by noise in 3D point cloud cable data, it is essential to apply a series of filtering algorithms to reduce noise and improve the overall quality of the 3D point cloud cable data [22]-[24].

Some scholars have studied 3D point cloud denoising algorithms to address issues such as high computational complexity, inaccurate feature extraction, and susceptibility to environmental obstacles in traditional point cloud segmentation techniques. Jia, C et al. proposed an outlier point cloud data denoising algorithm based on RGB-D information, which remaps and segments information such as light intensity and reflection characteristics from color images to effectively remove various outliers from image data [25]. Cheng, D et al. studied a denoising algorithm for lidar point cloud data (PCD). By projecting the 3D PCD onto a 2D plane and combining the proposed grid principal component analysis (PCA) technique with a ground-based stitching method for filtering, they achieved effective removal of noise from point cloud data [26]. Dong, S et al. demonstrated that the 3D synthetic aperture radar (SAR) point cloud reconstruction process is often affected by a large number of noisy scatter points. Therefore, they designed a K-nearest neighbor composite weighted filtering algorithm to improve point cloud data quality and enhance target recognition efficiency [27]. Wang, X et al. combined deep learning with filtering to form a PointFilterNet (PFN) point cloud denoising network, which automatically generates filtering denoising points through its excellent parameter learning capabilities, thereby progressively denoising the point cloud [28]. Regaya, Y et al. introduced unsupervised machine learning techniques for detecting noise in 3D point cloud data, namely Isolated Forests (If) and Elliptical Envelopes (EE). The proposed method demonstrated effective point denoising performance in scenarios heavily contaminated by noise [29]. Zou, B et al. employed farthest point weighted mean downsampling (FWD) to quickly simplify feature points in point cloud data, combined with a wavelet function bilateral filtering method (PWB) based on principal component analysis, achieving noise removal while preserving feature points, thereby enhancing image denoising accuracy [30]. For cable structure parameter extraction, the aforementioned point filtering, outlier filtering, and bilateral filtering schemes can filter out interference noise while maintaining good point cloud features. However, they also have limitations, such as the inability to automatically adjust parameters and the inability to remove noise at multiple scales in one go. Based on this, multi-filter algorithms can enhance the features of 3D point cloud cable data while effectively removing noise at multiple scales, providing a solid foundation for subsequent 3D point cloud cable segmentation and recognition, and thus hold significant research value.

To address the shortcomings of conventional point cloud filtering methods, this paper proposes a point cloud filtering algorithm that combines tensor voting and multi-scale normal vector estimation. Tensor voting is used to obtain high-frequency information from the point cloud, while multi-scale normal vector estimation is employed to extract noise planes from the high-frequency information point cloud to remove noise points, thereby obtaining the point cloud model. Based on this, the paper compares basic filtering methods and evaluates six filtering algorithms using visualization methods in different scenarios. Subsequently, a cable simulation model is established and simulation calculations are performed to validate the effectiveness of the proposed algorithm. Finally, an improved method is proposed to enhance cable structure, enabling enterprises to reduce costs and achieve economic benefits.

II. Multi-dimensional filtering algorithm for cable point cloud images

II. A. Acquisition of cable point cloud image data

II. A. 1) Basic Principles of Laser Triangulation

Multi-line laser measurement [31] is a non-destructive, non-contact measurement method based on the theory of laser triangulation. The process can be simply described as follows: a laser transmitter emits a laser beam onto the surface of the object to be measured, the laser beam is reflected by the surface of the object and received by a laser receiver, and then the position information of the object is calculated based on the triangular relationship formed by the angle of deviation of the light beam. Figure 1 shows a schematic diagram of the principle of laser triangulation measurement.

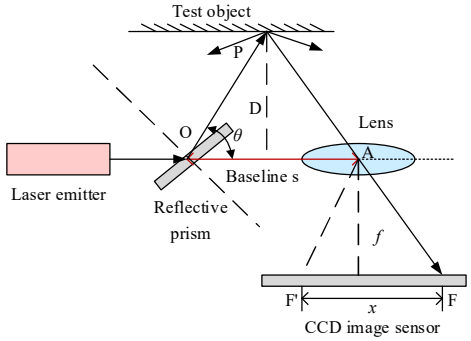

Figure 1: Schematic diagram of laser triangulation measurement principle

From the two similar triangles ΔOAP and $\Delta F'FA$ in the figure, the distance D from the object to the lens can be calculated using equation (1):

$$\begin{cases} x = \dfrac{f}{\tan\theta} \cdot \dfrac{N}{N'} \\ D = \dfrac{f \cdot s}{x} = \dfrac{s \cdot \tan\theta \cdot N'}{N} \end{cases} \tag{1}$$

In the equation, x is the distance from the center of the lens to the auxiliary point, f is the focal length of the lens, θ is the angle between the prism reflection point and the baseline, N and N' are the number of pixel units on the CCD imaging sensor between the auxiliary points F and F' and between the center of the lens and F', respectively, s is the distance between the prism reflection point and the lens focal point.

II. A. 2) Measurement principle of handheld laser scanners

A complete handheld laser scanner system generally consists of three parts: information input, data collection, and data processing output. The process of using a handheld scanner to perform 3D reconstruction of the object being measured can be described as follows: before scanning, the marker points on the surface of the object being measured are identified and a marker point library is constructed.

(1) Marker point library construction

Before scanning the workpiece, use the scanner to obtain the coordinate information of the marked points affixed to the surface of the object being measured or the external support structure under the reference (initial) viewing angle to construct the initial marked point library. Then, change the perspective to obtain the coordinate information of the marked points on the surface of the measured object or on the external support at different perspectives. Calculate the correspondence between the marked points at different perspectives and the existing marked points in the marked point library, and use methods such as singular value decomposition to obtain the rotation matrix R and translation matrix T for each viewpoint relative to the reference viewpoint. These rotation and translation matrices are then used to transform the marked points obtained from different viewpoints into the marked point database. This process is repeated by continuously changing viewpoints until all marked points are added to the marked point database, thereby obtaining a complete marked point database.

(2) Single-view point cloud acquisition and stitching

Let $P_w(X_w, Y_w, Z_w)$ denote a point in the world coordinate system, and let (X_c, Y_c, Z_c) and $(u, v, 1)$ are the points of P_w in the camera coordinate system and image coordinate system of a binocular measurement system, respectively. If the internal parameter matrix M_L of the camera is known, then (X_c, Y_c, Z_c) and $(u, v, 1)$ can be transformed using equation (2), while $P_w(X_w, Y_w, Z_w)$ and the point (X_c, Y_c, Z_c) can be transformed using equation (3).

$$Z_c \begin{bmatrix} u \\ v \\ 1 \end{bmatrix} = M_L \begin{bmatrix} X_c \\ Y_c \\ Z_c \\ 1 \end{bmatrix} \tag{2}$$

The relationship between the world coordinate system and the camera coordinate system can be determined by the spatial transformation matrix $M = [R \mid T]$ as follows:

$$\begin{bmatrix} X_c \\ Y_c \\ Z_c \\ 1 \end{bmatrix} = \begin{bmatrix} R_{3\times3} & T_{3\times1} \\ 0^T & 1 \end{bmatrix} \begin{bmatrix} X_w \\ Y_w \\ Z_w \\ 1 \end{bmatrix} \tag{3}$$

Substituting equation (2) into (3) yields the transformation relationship between a point in the world coordinate system and a point in the image coordinate system, calculated as shown in equation (4):

$$Z_c\begin{bmatrix} u \\ v \\ 1 \end{bmatrix} = M_L\begin{bmatrix} R_{3\times3} & T_{3\times1} \\ 0^T & 1 \end{bmatrix}\begin{bmatrix} X_w \\ Y_w \\ Z_w \\ 1 \end{bmatrix} \tag{4}$$

Let a point $P_w(X_w, Y_w, Z_w)$ in space be calculated according to equation (4) to obtain the coordinate points of the left and right cameras' image planes, which are (u_1, v_1) and (u_2, v_2), respectively, and the projection matrices of the left and right cameras are M_1 and M_2 in equation (5), respectively. Substituting equation (5) into equation (4) yields equation (6):

$$M_1 = \begin{bmatrix} m_{11}^1 & m_{12}^1 & m_{13}^1 & m_{14}^1 \\ m_{21}^1 & m_{22}^1 & m_{23}^1 & m_{24}^1 \\ m_{31}^1 & m_{32}^1 & m_{33}^1 & m_{34}^1 \end{bmatrix}, M_2 = \begin{bmatrix} m_{11}^2 & m_{12}^2 & m_{13}^2 & m_{14}^2 \\ m_{21}^2 & m_{22}^2 & m_{23}^2 & m_{24}^2 \\ m_{31}^2 & m_{32}^2 & m_{33}^2 & m_{34}^2 \end{bmatrix} \tag{5}$$

$$\begin{cases} \left(u_1 m_{31}^1 - m_{21}^1\right)X_w + \left(u_1 m_{31}^1 - m_{12}^1\right)Y_w + \left(u_1 m_{33}^1 - m_{13}^1\right)Z_w = m_{14}^1 - u_1 m_{34}^1 \\ \left(v_1 m_{31}^1 - m_{21}^1\right)X_w + \left(u_1 m_{31}^1 - m_{12}^1\right)Y_w + \left(u_1 m_{33}^1 - m_{23}^1\right)Z_w = m_{24}^1 - v_1 m_{34}^1 \\ \left(u_2 m_{31}^2 - m_{21}^2\right)X_w + \left(u_2 m_{31}^2 - m_{12}^2\right)Y_w + \left(u_2 m_{33}^2 - m_{13}^2\right)Z_w = m_{14}^2 - u_1 m_{34}^2 \\ \left(v_2 m_{31}^2 - m_{21}^2\right)X_w + \left(v_2 m_{31}^2 - m_{22}^2\right)Y_w + \left(v_2 m_{33}^2 - m_{23}^2\right)Z_w = m_{24}^2 - u_1 m_{34}^2 \end{cases} \tag{6}$$

Let point $q = [X_w, Y_w, Z_w]^T$ is the three-dimensional coordinate vector of the point P to be reconstructed. Rewriting equation (6) in the form $Kq = L$, equation (7) becomes the coordinate vector calculation method for the spatial scan point P.

$$q = (K^T K)^{-1} K^T L \tag{7}$$

Using equation (7), the three-dimensional data and marker point position information are obtained from the current viewpoint. The correspondence between the marker points in the current viewpoint and those in the marker point database is calculated, and then the rotation matrix R and translation matrix T in the global coordinate system based on this correspondence. The three-dimensional laser point cloud data calculated from the current viewpoint is then transformed into the global coordinate system according to this rotation and translation relationship. This process is repeated until the entire three-dimensional morphology of the measured object is obtained.

II. B.Point cloud data preprocessing

II. B. 1) Point Cloud Simplification

As point cloud acquisition devices continue to evolve and improve, their performance becomes increasingly superior. During the process of using a scanner to obtain point cloud data for cable joints, tens of thousands of data points are generated in a short period of time. This results in issues such as large data volumes, redundancy, and uneven point density in the raw point cloud. The high redundancy of the data not only increases the hardware requirements and processing time for point cloud processing but also reduces the effectiveness of subsequent point cloud processing. Therefore, to improve algorithm processing speed and measurement accuracy, it is necessary to remove redundant points from the raw point cloud data before computation. This ensures that point clouds with lower data volumes can still accurately represent object features, achieving the same or similar results as those with larger point cloud volumes. This process is known as point cloud simplification.

II. B. 2) Point Cloud Smoothing

Point cloud normal vectors are an important feature of point cloud data. This paper uses the classic normal vector estimation method, principal component analysis (PCA) algorithm, to estimate the normal vectors of cable joint point clouds. When estimating the normal vector for any point $p_r(x_r, y_r, z_r)$ in the point cloud using the PCA algorithm, the covariance matrix R is constructed using its m neighbors according to Equation (8), and singular value decomposition is used to obtain the eigenvalues and eigenvectors of R. The eigenvector v_0 corresponding to the smallest eigenvalue λ_0 of matrix R is the normal vector of point $p_r(x_r, y_r, z_r)$.

$$\begin{cases} \overline{p} = \frac{1}{m}\sum_{r=1}^{m} p_r \\ R = \frac{1}{m}\sum_{r=1}^{m}(p_r - \overline{p})(p_r - \overline{p})^T \\ R \cdot \overline{v}_r = \lambda_r \cdot \overline{v}_r, r \in \{0,1,2\} \end{cases} \tag{8}$$

In the equation: m is the number of neighborhood points used in estimating the normal vector at point p_r, $\overline{p}$ is the three-dimensional centroid of the neighborhood points participating in the normal vector estimation, and v_r represents the eigenvector of eigenvalue λ_r. Equation (9) shows how parameter D is calculated:

$$\begin{cases} D = -(a\overline{x} + b\overline{y} + c\overline{z}) \\ \overline{x} = \frac{1}{m}\sum_{r=1}^{m} x_r, \overline{y} = \frac{1}{m}\sum_{r=1}^{m} y_r, \overline{z} = \frac{1}{m}\sum_{r=1}^{m} z_r \end{cases} \tag{9}$$

In the formula, $\overline{x}$, $\overline{y}$, and $\overline{z}$ are the mean values of the coordinates of points x, y, and z in the neighborhood of point p_r, respectively.

The direction of the normal vector estimated using the PCA algorithm is ambiguous. To make its direction satisfy the required direction, it needs to be reoriented. If the normal vector $\overline{N}_r(a,b,c)$ of point $p_r(x_r,y_r,z_r)$ does not satisfy formula (10), it will be reoriented.

$$\overline{N}_r(V_p - p_r) > 0 \tag{10}$$

In the formula: $\overline{N}_r$ is the normal vector of point $p_r(x_r,y_r,z_r)$ and V_p is the viewpoint.

II. C.Improved laser point cloud filtering algorithm

II. C. 1) Double Tensor Voting Method

The point cloud model obtained through a laser scanner consists mostly of low-frequency information points. Filtering the entire point cloud is not only computationally expensive but also risks damaging the point cloud model. This paper employs a dual tensor voting method to first extract high-frequency information points (including feature points and noise points) from the point cloud, then apply filtering to the high-frequency information points to reduce computational load while improving filtering accuracy. The normal vector tensor voting matrix T_n can be expressed as:

$$T_i^n = \frac{1}{\sum_{j\in K_i} w_{i,j}^n} \sum_{j\in K_i} w_{i,j}^n \left(n_{i,j} n_{i,j}^T\right) \tag{11}$$

In the formula: $n_{i,j}$ denotes the normal vector of the j th nearest neighbor point of sampling point P_i; $w_{i,j}^n$ denotes the weight of the normal vector tensor voting matrix, which can be expressed as:

$$w_{i,j}^n = \exp\left(-\left\|P_i - P_{i,j}\right\|_2 \Big/ 2\sigma^2\right) \tag{12}$$

In the equation, σ denotes the average distance between the sampling point P_i and its neighboring points. From equation (12), it can be seen that the farther the distance between the sampling point P_i and its j th neighboring point, the smaller the value of $w_{i,j}^n$.

The point tensor voting matrix T_p can be expressed as:

$$T_i^p = \frac{1}{\sum_{j\in K_i} w_{i,j}^p} \cdot \left\{ \sum_{j\in K_i} w_{i,j}^p \left[\left(p_{i,j} - \overline{p}\right)\left(p_{i,j} - \overline{p}\right)^T \right] \right\} \tag{13}$$

In the equation: $p_{i,j}$ denotes the direction vector between sampling point P_i and its j th nearest neighbor point; $\overline{p}$ denotes the average value of all $p_{i,j}$; $w_{i,j}^p$ denotes the weight of the point tensor voting matrix, which can be expressed as:

$$w_{i,j}^{p} = \exp\left(-\left\|n_i - n_{i,j}\right\|_2 / 2\sigma^2\right) \tag{14}$$

The eigenvalues of the tensor matrix are λ_1, λ_2, and λ_3, corresponding to the eigenvectors e_1, e_2, and e_3, where $\lambda_1 \geq \lambda_2 \geq \lambda_3$.

Based on the relationship between the eigenvalues of the three-dimensional tensor, the positions of the points can be determined. If $\lambda_1 \approx \lambda_2 \approx \lambda_3 \approx 0$, then the point is a surface point; if $\lambda_1 \geq \lambda_2 \approx \lambda_3 \approx 0$, then the point is a boundary point; if $\lambda_1 \geq \lambda_2 \geq \lambda_3 \approx 0$, then the point is a corner point or an outlier.

II. C. 2) Multi-scale normal vector filtering

Filter the extracted high-frequency information. Discrete noise points are easy to remove, but dense planar noise points are difficult to remove using traditional methods, especially those close to the model, which can cause significant damage to the model. Based on the RANSAC method, use two sets of K values of different sizes to estimate the normal vector of the model (K value represents the number of K nearest neighbors).

To preserve the high-frequency point cloud while avoiding damage to the existing planes in the model, this paper uses the normal vectors estimated with larger K values for tensor voting to extract high-frequency information, and then uses the normal vectors estimated with smaller K values for plane extraction.

For each point in the extracted high-frequency point cloud, the dot product is calculated between its normal vector and those of its nearest neighbors. A larger value indicates a smaller angle between the normal vectors of the two points, suggesting that their directions are consistent. To increase the influence of nearby points and facilitate threshold selection, this paper adopts a linear weighting method: the greater the distance between two points, the smaller the weight assigned, ensuring that the sum of the weights of all neighboring points is 1. The flatness d_i of the plane formed by the i th sampling point and its neighboring points can be expressed as:

$$d_i = \sum_{j \in K_i} \left[(n_i \cdot n_{i,j}) * (l_{i,K-j}) \right] \tag{15}$$

In the formula, $l_{i,K-j}$ denotes the distance between the i th sampling point and its $K-j$ th nearest neighbor point.

II. C. 3) Curvature filtering

After removing dense planar noise, use a combination of curvature and threshold (the threshold is selected to remove the maximum value of all noise points) to remove points greater than the threshold and further filter the feature point cloud. The curvature of the surface can be expressed as

$$C_{v,i} = \frac{\lambda_3}{\lambda_1 + \lambda_2 + \lambda_3} \tag{16}$$

The three eigenvalues have already been calculated in the process of calculating the normal vector, so there is no need to calculate them again. Calculate the curvature while calculating the normal vector.

II. D.Evaluation of filtering algorithms

II. D. 1) Filtering experiment based on statistical histograms

To avoid noise data affecting the results of the statistical histogram, statistical filtering is first used to remove noise, while downsampling is performed to improve the speed of subsequent processing. The processed point cloud is divided into a grid with a side length of r on the XoY plane, and its z coordinate span is used as the basis for coloring.

To select a reasonable threshold for filtering, a histogram analysis is performed on the z axis span of this section, with the results shown in Figure 2. It can be clearly seen that the statistical histogram is divided into two parts by the boundary of 11-16: the left half represents areas with elevations less than 11, corresponding to the ground surface grid; the right half represents areas with elevations greater than 16, corresponding to power lines and towers.

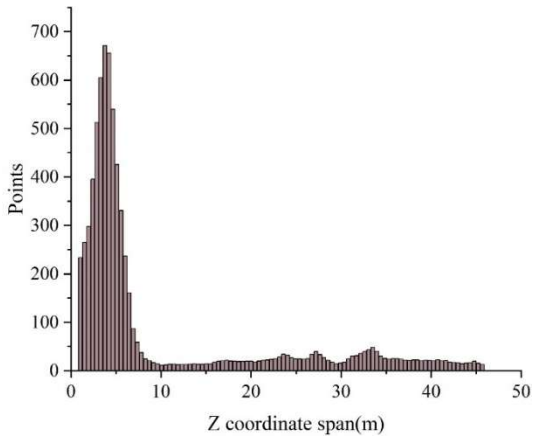

Figure 2: Point cloud XoY grid division z span distribution map

To further validate the conclusions drawn from this observation, the power lines and towers were manually removed from this part of the point cloud, and then a histogram analysis was performed, yielding the results shown in Figure 3. As the power lines and towers were removed, the grid with a large elevation span also disappeared.

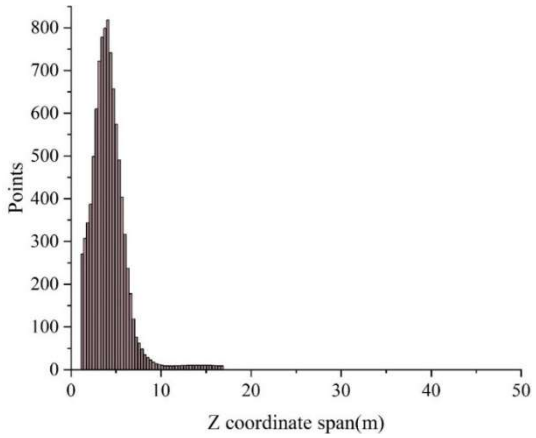

Figure 3: Z-span distribution map of XoY grid division of point cloud ground part

By comparing Figures 2 and 3, it can be seen that the ground surface, i.e., the grid with a low span, is mainly concentrated in the range of 0-16m. In the power inspection point cloud, there is a significant difference in elevation span between the ground surface and the power facility parts. Therefore, by filtering out the points with smaller height differences in the left half, the majority of ground features can be filtered out, significantly improving the efficiency of subsequent cable and tower extraction. Therefore, the key lies in finding an appropriate method to divide the data.

By observing the distribution of the histogram, it can be seen that in the sections with smaller height differences, the differences between adjacent statistical values are significant, and the gradient changes are obvious; whereas in the sections with larger height differences, each height is relatively small, and the gradient changes are not obvious, with a noticeable abrupt change at the x-coordinate of 11. To capture this change, the gradient tool can be used. By calculating the gradient of the statistical histogram, the results shown in Figure 4 are obtained. Clearly, the oscillating portion in the figure corresponds to the left side of the statistical histogram, while the stable portion is close to 0, corresponding to the right half of the statistical histogram.

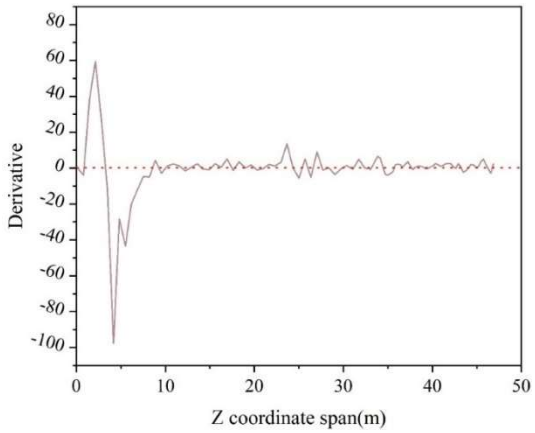

Figure 4: Gradient of z span distribution map of point cloud xoy grid division

At this point, a statistical analysis of the gradient values is performed to obtain their mean $mean$ and standard deviation std. Points on the grid z axis whose spans fall outside the range of $mean \pm std$ are classified as terrain points and can be directly filtered out, leaving the remaining points as the grid cells containing the power corridor. Based on the aforementioned steps, the bottom point cloud features of the power corridor section are similar to those of the removed terrain features. Therefore, by removing points within the span range of general terrain features from the bottom, the remaining points represent the more ideal cable section.

Statistical filtering downsampling and histogram filtering are applied to the original point cloud. The changes in point cloud size during processing are shown in Table 1. The data in the table further indicate that the statistical histogram-based filtering method effectively filters out ground features, significantly increasing the proportion of cable and tower features in the point cloud (from 3.349% to 74.476%) ; simultaneously, the filtering process results in only minimal loss of cable and tower sections ($\frac{6124-6072}{6124}=0.849\%$).

Table 1: The amount of data changes in the point cloud filtering process

Point cloud	Total points	Number of cables and poles	Cable and tower ratio
Initial cloud	3891309	24091	0.619%
Drop sampling point cloud	182847	6124	3.349%
Histogram filter point cloud	8153	6072	74.476%

In summary, the process of filtering power inspection point clouds using elevation difference statistical histograms is as follows:

(1) First, use statistical filtering to remove noise.

(2) Divide the point cloud into XoY grids.

(3) Perform histogram statistics on the z-coordinate range of each grid.

(4) Calculate the first derivative of the histogram, compute the mean and standard deviation of the first derivative, and extract the points corresponding to $(mean-std，\ mean+std)$ as the output.

II. D. 2) Quantitative Analysis

The accuracy rates of the six filtering algorithms—ROR, SOR, DROR, DSOR, DDIOR, and the algorithm proposed in this paper—under different scenarios are shown in Figure 5. (a) and (b) show the accuracy rates of each filtering algorithm in noisy and noise-free scenarios, respectively.

By observing Figure 5(a), it can be seen that the accuracy of DROR is 0.981524, the highest among all filtering algorithms. The accuracy of DDIOR is higher than that of DSOR. As an improved method, the accuracy of the proposed algorithm is second only to DROR, at 0.977992. Although the accuracy of the proposed algorithm lags behind DROR, it still holds an advantage over other filtering algorithms.

By observing Figure 5(b), it can be seen that the accuracy of DSOR is 0.973558, the highest among existing filtering algorithms. As an improved method, the accuracy of the proposed algorithm is higher than that of DSOR, specifically 0.979663.

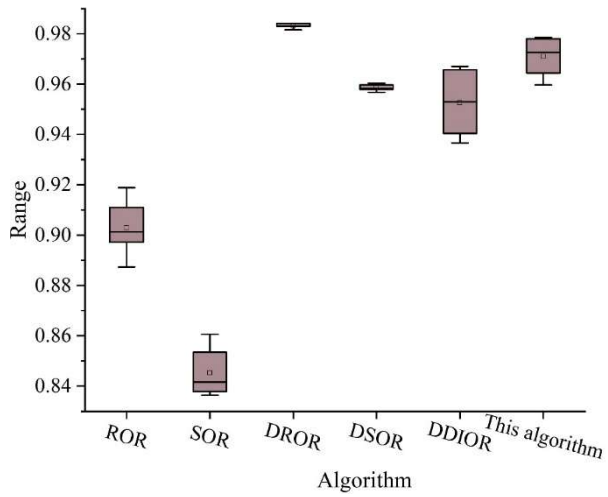

(a) Accuracy of each filtering algorithm in noiseless scene

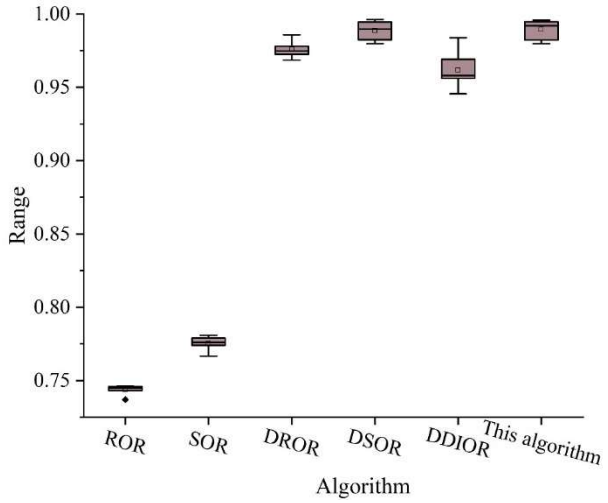

(b) Accuracy of each filtering algorithm in noiseless scenario

Figure 5: Accuracy for each filtering method

By analyzing the experimental results in Figure 5, it can be observed that the filtering accuracy of the filtering algorithm in noisy scenarios is less stable than in noise-free scenarios. This indicates that the robustness of the filtering algorithm in noisy scenarios is reduced compared to noise-free scenarios. It is speculated that this phenomenon is caused by the inability to effectively filter out noise points generated in noisy scenarios. As an improved method, although the algorithm in this paper also shows a decline in noisy environments, it is the least affected among all filtering methods and demonstrates the best robustness in practical applications.

II. D. 3) Algorithm Efficiency

Table 2 shows the average processing times of six filtering algorithms—ROR, SOR, DROR, DSOR, DDIOR, and the algorithm proposed in this paper—in two scenarios: noisy and noise-free. In both scenarios, ROR had the shortest processing time, at 98.2759 milliseconds (noisy scenario) and 105.392 milliseconds (noise-free scenario); the proposed algorithm follows, with 108.841 milliseconds (noisy scenario) and 147.727 milliseconds (noisy scenario); DROR has the longest processing time, significantly higher than other filtering algorithms, with 5179.147 milliseconds (noisy scenario) and 4793.872 milliseconds (noisy scenario).

Table 2: Algorithmic efficiency for each filtering method

Filtering algorithm	Noise scene (ms)	Noiseless scene (ms)
ROR	98.2759	105.392
SOR	121.052	158.114
DROR	5179.147	4793.872
DSOR	109.951	147.784
DDIOR	109.725	168.203
This algorithm	108.841	147.727

By analyzing the experimental results in Table 2, it can be observed that the ROR algorithm achieves the highest efficiency in both noisy and noise-free scenarios, as its algorithmic time complexity is relatively low, being; the algorithmic time complexities of SOR, DSOR, and DDIOR are $O(\log n)$; therefore, their algorithmic efficiency is lower than that of ROR; The processing time of DROR is significantly higher than that of other filtering algorithms. This is because the method requires traversing all points in the data and continuously iterating the search radius. Even after preprocessing the point cloud data using a $kd-tree$, the algorithm's time complexity can only be reduced to $O(n\log n)$. Thus, the more complex algorithm structure results in DROR requiring more computational resources, leading to longer processing times. This efficiency issue becomes more pronounced when dealing with large point cloud datasets. As an improved method, the algorithm proposed in this paper also has a time complexity of $O(\log n)$;

however, its processing time remains slightly lower than that of statistical-based filtering algorithms such as SOR, DSOR, and DDIOR. Additionally, due to its ability to effectively reduce computational load, the efficiency advantage of this algorithm further increases as the size of the point cloud dataset grows.

III. Extraction of cable structural parameters based on point clouds

III. A. Diameter extraction

III. A. 1) Cable diameter calculation based on cylindrical fitting

The cable diameter calculation algorithm based on cylindrical fitting mainly consists of two parts. First, the cable is divided into supervoxels to obtain cable segments. Second, the divided cable segments are fitted with cylinders to obtain the diameter of the cylinders. Figure 6 shows the flowchart of this algorithm.

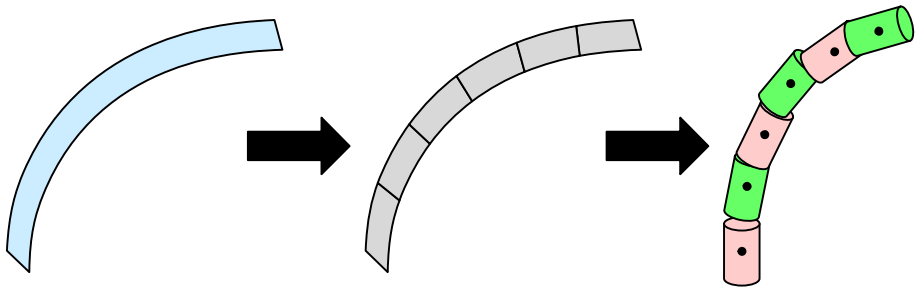

Figure 6: The flowchart of the diameter calculation algorithm based on cylindrical fitting

(1) Hypervoxel segmentation. First, hypervoxel clustering is performed on the cable point cloud obtained from the 3D dense reconstruction system to obtain uniform cable segments. Hypervoxel clustering is performed on the cable point cloud based on distance, and the adjacency graph information and the hypervoxels themselves are visualized.

(2) Cylinder fitting. After supercell clustering, uniform cable segments are obtained, and one point cloud segment is selected for cylinder fitting.

III. A. 2) Cable diameter calculation based on point cloud projection

The cable diameter calculation algorithm based on point cloud projection mainly consists of two parts. First, through octree map search, a portion of the cable point cloud is obtained and projected onto a two-dimensional plane. Second, through directed bounding boxes, the cable diameter is calculated.

First, the cable point cloud is converted into an octree graph to extract a portion of the cable point cloud. The octree resolution is set to a large value to ensure that each octree node contains as many point cloud points as possible. A point is randomly selected from the cable point cloud, and the octree node containing that point is calculated. All point cloud points in that node are extracted to obtain a portion of the cable. The resulting cable segment is projected onto a two-dimensional plane, represented as:

$$Ax + By + Cz + D = 0 \tag{17}$$

Let $A = 0$, $B = 0$, $C = 1$, $D = 0$, then the projection of the cable point cloud is obtained in the XOY plane. Then, the cable point cloud segment is enclosed by the minimum bounding box to obtain the diameter of the cable, which can effectively reduce the error when calculating the diameter of the bent cable.

After the minimum bounding box successfully encloses the cable point cloud, two valid values are obtained: width and height. The width represents the length of the bounding box, and the height represents the width of the bounding box, i.e., the diameter of the cable.

III. B. Length parameter extraction

III. B. 1) Optimal Path Generation

To improve search efficiency, the point cloud is converted into an octree map for searching. The octree resolution is set to the cable diameter, making the constructed octree more regular and easier to use with the $A*$ pathfinding algorithm to find the optimal path. When using the $A*$ pathfinding algorithm to find the optimal path in the octree, it is necessary to determine the starting point and endpoint. First, extract the octree nodes containing the point cloud points. Then, traverse the extracted octree nodes, calculate the distance between each pair of nodes, and identify the two octree nodes with the maximum Manhattan distance as the starting point and endpoint for the $A*$ pathfinding algorithm.

$$m_{dist} = \left|x_{p_j} - x_{p_i}\right| + \left|y_{p_j} - y_{p_i}\right| + \left|z_{p_j} - z_{p_i}\right| \tag{18}$$

Among these, m_{dist} is the maximum length obtained by traversing the entire octree, p_j is the endpoint of the octree corresponding to this maximum length, p_i is the starting point of the octree corresponding to this maximum length, and (x, y, z) represents the corresponding coordinates. Using the starting point and endpoint, perform an $A*$ search. The core of the $A*$ algorithm lies in the cost function, expressed as follows:

$$f(k) = g(k) + h(k) \tag{19}$$

where $f(k)$ denotes the distance from the path starting point p_i through the current node k to the path endpoint p_j, $g(k)$ denotes the distance from the path starting point p_i to the current node k, and $h(k)$ denotes the distance from node k to the octree endpoint p_j.

The specific implementation process of the improved $A*$ three-dimensional search octree optimal path algorithm is as follows:

(1) First, starting from the octree starting point p_i, search for the 26 adjacent cubes containing point cloud points that have not been visited.

(2) Find the nearest octree node with the smallest cost estimate function value $f(k)$, and use this node as the new path starting point. Repeat step (1) to search for the surrounding nodes of this node.

(3) If the current octree node is the path endpoint, output the optimal path.

III. B. 2) Skeleton Point Extraction

For each octree node in the optimal path, use the following formula to calculate the point cloud point closest to the center of the octree node.

$$x_m = x_{key[i]} \times height + x_{\min} \tag{20}$$

Among them, $key[i]$ represents the octree node in the i th optimal path, (x, y, z) represents the spatial coordinates, and $(x_{\min}, y_{\min}, z_{\min})$ represents the coordinates of the initial position point cloud points in the entire point cloud. Using formulas (18), (19), and (20), the center point coordinates (x_m, y_m, z_m) of the octree node are calculated. By calculating the distance between the points, the coordinates of the skeleton point closest to the center point are obtained.

III. B. 3) B-spline curve fitting

After obtaining the skeleton points of the cable, in order to ensure that the shape of the skeleton obtained by the algorithm matches the shape of the cable, thereby improving the accuracy of the length calculation algorithm, this paper does not directly connect the skeleton points, but instead uses the B spline fitting algorithm for curve fitting. The B -spline curve fitting algorithm includes approximation fitting and interpolation fitting algorithms. The approximation fitting algorithm does not pass through the skeleton points when fitting the curve. Since this paper requires the calculation of the curve's expression, the B -spline interpolation fitting algorithm is selected.

First, the control points of the B -spline curve are obtained from the skeleton points, and then the equation of the quadratic B -spline curve is calculated. Every three discrete points form a curve. First, the skeleton points are smoothed onto the B -spline curve. Then, a specified number of points are uniformly inserted between the skeleton points. Finally, the analytical expression of the quadratic B-spline curve is obtained, which can be expressed as:

$$P(t) = \frac{1}{2}(1-t)^2 P_0 + \frac{1}{2}(-2t^2 + 2t + 1)P_1 + \frac{1}{2}t^2 P_2 \tag{21}$$

where P_0, P_1, and P_2 are the three skeleton points that generate the quadratic B spline curve, and t is the parameter of the curve. Divide the curve parameter t into k equal parts, with t starting from 0 and the interval dt up to $k*dt$. To ensure that the endpoints of the quadratic B -spline curve correspond to the endpoints of the first control points, i.e., to make the two endpoints of the entire curve coincide with the starting point P_0 and the endpoint P_n, new points are constructed with P_0 and P_n as midpoints: $PP_1 = 2*P_0 - P_1$ and $PP_2 = 2*P_n - P_{n-1}$ to replace P_0 and P_n, respectively.

III. B. 4) Numerical integration calculation length

After curve fitting is completed, the derivative of the quadratic B-spline curve in the parameter interval $[t_i, t_{i+1}]$ is:

$$P'(t) = (t-1)P_0 + (1-2t)P_1 + tP_2 \tag{22}$$

For any t in the domain, the value of $P'(t)$ can be obtained. Using the Gauss quadrature formula in numerical integration, the arc length of the corresponding curve in this interval can be calculated. The integration interval of the Gauss-Legendre formula is $[0,1]$ and when the parameter interval is $[t_1, t_2]$, the formula is:

$$\int_{t_2}^{t_1} f(x)dx = \frac{t_2 - t_1}{2}\int_{-1}^{1} f\left(\frac{t_2 - t_1}{2}u + \frac{t_2 + t_1}{2}\right)|du| \tag{23}$$

Using the Gauss-Legendre formula, convert the integral of an indefinite interval into a definite integral interval for calculation, and obtain the arc length of the quadratic $B-$ spline curve L on the interval $[t_1, t_2]$.

$$L(t_1, t_2) = \int_{t_2}^{t_1} |P'(t)|dt = \frac{t_2 - t_1}{2}\int_{-1}^{1} \left|P'\left(\frac{t_2 - t_1}{2}x + \frac{t_2 + t_1}{2}\right)\right|dx \tag{24}$$

After obtaining the arc length L of a quadratic $B-$ spline curve, add up all the curve lengths in the cable. The total arc length S is obtained as $S = L_1 + L_2 + \cdots + L_n$, where n is the total number of curves.

III. C. Simulation Analysis

III. C. 1) Simulation Model

The inner conductor of a single cable consists of 2,841 strands of 0.3 mm diameter tin-plated soft copper wire. During simulation, these are replaced with copper wire of 7.27531 mm radius (cross-sectional area 200 mm²). The cable insulation layer is made of 3 mm thick temperature-resistant silicone rubber, which is replaced during simulation with rubber material having a dielectric constant of 3 and a volume conductivity of 10–15 S/m. The cable protective layer is made of 2 mm thick flame-retardant cross-linked polyolefin extrusion. In simulation, it is replaced by polyethylene material with a dielectric constant of 2.25 and a dielectric loss factor of 0.01. The simulation model of the cable established in Q3D is shown in Figure 7.

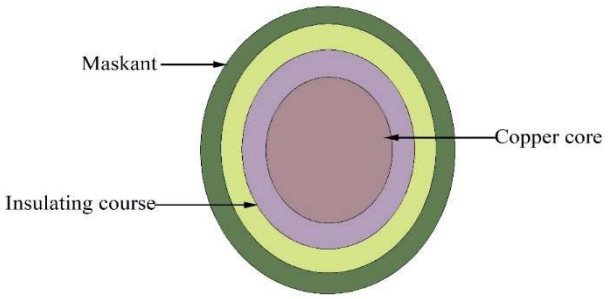

Figure 7: Simulation model of single cable

III. C. 2) Simulation Calculations

After establishing the model, four layout configurations were modeled: three-phase triangular layout, parallel layout, parallel layout with cable diameters spaced apart, and parallel layout with cable diameters spaced apart by twice the diameter. Based on the three-phase PWM drive principle, the entire system is considered as a whole. At each switching conduction moment, current flows into one phase cable and out of the other two phases. Therefore, during simulation calculations, current is set to flow into one phase cable and out of the other two phases.

(1) Diamond-shaped layout

The three-phase cables are arranged in a diamond-shaped layout as shown in Figure 8. Cable A is loaded with the signal, and cables B and C are loaded with the reference signal ground (in the software, the default relationship between these two is that one current flows in and one flows out). The calculation results are shown in Table 3.

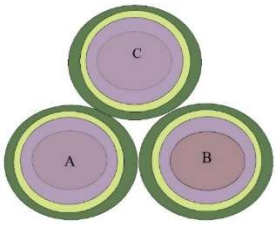

Figure 8: Cable layout in the shape of a character

Table 3: Calculation result

Transmission parameter	Signal A	Transmission parameter	Signal A
C(pF/m)	43.214	R(ohm/m)	0.011742
G(mSie/m)	3.7357E-3	L(nH/m)	382.54

(2) Parallel straight lines laid out side by side

The three-phase cables are laid out in a zigzag pattern as shown in Figure 9. In the first loading method, the A-phase cable is loaded as the reference ground, and the BC-phase cables are loaded with signals. In the second loading method, the AC-phase cables are loaded as the reference ground, and the B-phase cables are loaded with signals. The calculation results are shown in Table 4.

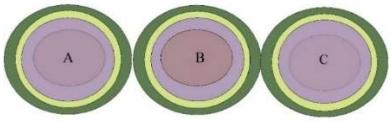

Figure 9: Parallel lines are laid out side by side

Table 4: Calculation result

Loading mode	C(pF/m)	G(mSie/m)	R(ohm/m)	L(nH/m)
First loading	33.3759	3.1847E-5	0.014532	486.26
The second type of loading	51.4318	5.1271E-5	0.009986	327.75

(3) Parallel straight line spacing cable diameter layout

The three-phase cables are arranged in parallel straight lines with cable diameter spacing as shown in Figure 10. Cable A carries the signal, and cables BC carry the reference signal ground (the default current flow relationship between the two in the software), and the calculation results are shown in Table 5.

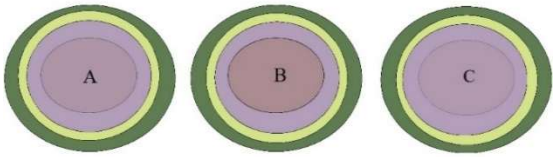

Figure 10: Parallel straight line spacing cable diameter layout

Table 5: Calculation result

Loading mode	C(pF/m)	G(mSie/m)	R(ohm/m)	L(nH/m)
First loading	20.283	3.7514E-5	0.011228	731.72
The second type of loading	25.71	7.183E-5	0.0097159	547.73

(4) Parallel straight line spacing of 2 times the cable diameter layout

The three-phase cables are arranged in parallel straight lines with a spacing of the cable diameter, as shown in Figure 11. Cable A carries the signal, and cables BC carry the reference signal ground. The calculation results are shown in Table 6.

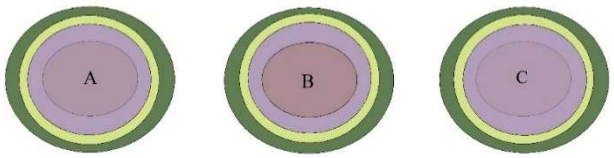

Figure 11: After laying parallel straight lines at a distance of twice the cable diameter

Table 6: Calculation result

Loading mode	C(pF/m)	G(mSie/m)	R(ohm/m)	L(nH/m)
First loading	15.853	2.5783E-5	0.0099098	857.19
The second type of loading	19.974	3.7761E-5	0.0095471	673.28

According to the calculation results, it can be seen that when cables are arranged in a triangular pattern, the capacitance between cables is maximum, but the inductance is minimum; when cables are arranged with a spacing of twice the cable diameter, the capacitance is minimum, but the inductance is maximum. From the perspective of electromagnetic field principles, this is because increasing the cable spacing increases the coupling distance, thereby reducing the coupling capacitance; increasing the cable spacing also increases the current loop, thereby increasing the loop inductance.

After establishing the model, the transmission line parameters per unit length of power cables can be quickly calculated. Comparing the results of the four calculation methods with those obtained using the improved method, the results are consistent in magnitude, thereby validating the effectiveness of the improved method to a certain extent.

III. D. Power cable structure improvement plan

III. D. 1) Power cable structure improvement plan

Currently, the average resistance of the copper conductors in three-core power cables produced by cable companies is 12.5 Ω /km, as the standard maximum conductor resistance is 13.3 Ω /km. this indicates that improvements can be made to the diameter of the copper conductor strands. By reducing the diameter of the copper strands and altering the number of strands, the outer diameter of the conductor stranding will decrease, slightly increasing the conductor resistance but remaining within the maximum resistance limit, thereby reducing copper consumption.

With the company's assistance, improvements were made to the single-wire diameter of the copper conductors in power cables, and production of the improved power cables was carried out. The specific test results are compared as shown in Table 7.

As can be seen from the table, when only the single-wire diameter was changed, the measured conductor resistance increased slightly but still did not exceed the maximum conductor resistance, meeting production standards. From the measured copper weight, copper consumption was also reduced, yielding certain economic benefits for the company.

Table 7: Comparison of test results before and after

Parameter	Power cables before improvement	Improved power cable
sectional area /mm^2	1.7	1.7

radical / root	30	30
Single filament diameter/mm	0.27	0.251
Twisted outer diameter/mm	1.8	1.8
Quality of copper/(kg·km^{-1})	14.2764	12.8543
Calculate the cross-sectional area/mm^2	1.79161	1.37969
Average conductor resistance/(Ω·km^{-1})	12.842	13.486

III. D. 2) Improvement plan for strand pitch

The average stranding pitch for power cables produced by the cable company is currently around 170. This paper aims to reduce the stranding pitch of power cables to decrease their resistance values and analyze copper usage. With the assistance of the cable company, some power cables with smaller stranding pitches were produced. Resistance tests were conducted on the improved power cables and compared with those currently produced by the company, with specific data shown in Figure 12.

As shown in the figure, the average stranding pitch of the improved power cables is 167. The reduction in stranding pitch increases the outer diameter of the power cables, leading to an increase in the nominal cross-sectional area and a decrease in conductor resistance. The improved power cables' stranding outer diameter and conductor resistance are both within the standard range, so improving the stranding pitch of power cables is feasible.

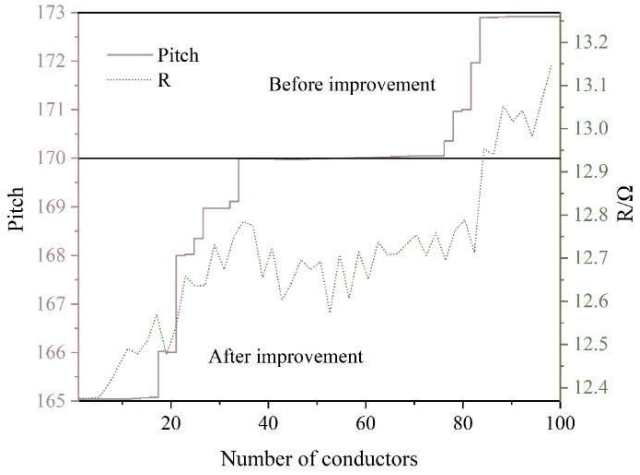

Figure 12: Comparison chart of cable improvement twist before and after

IV. Conclusion

This paper proposes a point cloud filtering algorithm that combines dual tensor voting and multi-scale vector estimation. The proposed algorithm is used to perform parameter processing on scanned cable point cloud images. Numerical experiments are conducted to analyze basic filtering methods, and the proposed method is evaluated under different noise conditions. The results show that basic filtering methods can significantly reduce the amount of ground point data while selectively retaining the cable region, effectively improving the efficiency and accuracy of subsequent cable extraction. As an improved algorithm, it demonstrates excellent overall performance in both noisy and noise-free scenarios, and achieves the highest overall performance compared to other filtering algorithms in noise-free scenarios. Subsequently, a common distributed parameter model for cable transmission lines was established and simulated. The improved method can provide verification and support for the extraction of transmission line parameters in applications such as power cable communication. Through the proposed method, improvement schemes were identified, and optimal structural parameters were found.

Funding

Science and Technology Project of State Grid Shaanxi Electric Power Co., Ltd.: Research on Intelligent Detection Technology of Cable Geometric Parameters Based on 3D Laser Scanning (5226WN240005).

References

[1] Siirto, O., Vepsäläinen, J., Hämäläinen, A., & Loukkalahti, M. (2017). Improving reliability by focusing on the quality and condition of medium-voltage cables and cable accessories. CIRED 24, 2017(1), 229-232.

[2] Wang, W., Yan, X., Li, S., Zhang, L., Ouyang, J., & Ni, X. (2021). Failure of submarine cables used in high-voltage power transmission: Characteristics, mechanisms, key issues and prospects. IET Generation, Transmission & Distribution, 15(9), 1387-1402.
[3] Song, Y., Chen, W., Wan, F., Zhang, Z., Du, L., Wang, P., ... & Huang, H. (2022). Online multi-parameter sensing and condition assessment technology for power cables: A review. Electric Power Systems Research, 210, 108140.
[4] Wei, C., Tan, L., Zhang, K., Chen, S., Xu, C., & Qu, Z. (2022, September). Research on critical technology application of power electronic technology in substation cable laying. In 2022 International Conference on Electronics and Devices, Computational Science (ICEDCS) (pp. 50-53). IEEE.
[5] Gulski, E., Jongen, R., & Parciak, J. (2020). Quality Management of Transmission Power Cables for Safe and Reliable Grid Operation. Wiadomości Elektrotechniczne, 88.
[6] Pattabi, P., Naderian Jahromi, A., Lo, S., Martin-Sturmey, K., & Bhagwandass, N. (2023). Practical Approach to Underground Distribution Power Cable Fleet Management. Energies, 16(8), 3526.
[7] Jongen, R., Quak, B., Gulski, E., Cichecki, P., & de Vries, F. (2012, September). On-site testing and diagnosis of long medium voltage cables. In 2012 IEEE International Conference on Condition Monitoring and Diagnosis (pp. 659-662). IEEE.
[8] Zhou, X., Chen, Q., Lyu, S., & Chen, H. (2022). Mapping the buried cable by ground penetrating radar and gaussian-process regression. IEEE Transactions on Geoscience and Remote Sensing, 60, 1-12.
[9] Li, X., Gao, C., Guo, Y., He, F., & Shao, Y. (2019). Cable surface damage detection in cable-stayed bridges using optical techniques and image mosaicking. Optics & Laser Technology, 110, 36-43.
[10] Hou, S., Dong, B., Wang, H., & Wu, G. (2020). Inspection of surface defects on stay cables using a robot and transfer learning. Automation in Construction, 119, 103382.
[11] Nan, Z., Xuhong, H., Wei-hao, X., & Shengping, T. (2022, November). Research on Cable Surface Quality Inspection System and Method Based on Image Processing Technology. In International Conference on Advanced Intelligent Systems and Informatics (pp. 370-380). Cham: Springer International Publishing.
[12] Jo, B. W., Lee, Y. S., Kim, J. H., & Yoon, K. W. (2018). A review of advanced bridge inspection technologies based on robotic systems and image processing. International Journal of Contents, 14(3).
[13] Wu, G., Yu, M., Shi, W., Li, S., & Bao, J. (2020). Image recognition in online monitoring of power equipment. International Journal of Advanced Robotic Systems, 17(1), 1729881419900836.
[14] Ghaforian, A., Duggan, P., & Lu, L. (2025). A Comprehensive Review of Cable Monitoring Techniques for Nuclear Power Plants. Energies, 18(9), 2333.
[15] Yang, L., Fan, J., Liu, Y., Li, E., Peng, J., & Liang, Z. (2020). A review on state-of-the-art power line inspection techniques. IEEE Transactions on Instrumentation and Measurement, 69(12), 9350-9365.
[16] Qin, X., Wu, G., Ye, X., Huang, L., & Lei, J. (2017). A novel method to reconstruct overhead high-voltage power lines using cable inspection robot LiDAR data. Remote sensing, 9(7), 753.
[17] Li, S., Cao, B., Li, J., Cui, Y., Kang, Y., & Wu, G. (2023). Review of condition monitoring and defect inspection methods for composited cable terminals. High Voltage, 8(3), 431-444.
[18] Shen, Y., Yang, Y., Jiang, J., Wang, J., Huang, J., Ferreira, V., & Chen, Y. (2023). A novel method to segment individual wire from bundle conductor using UAV-LiDAR point cloud data. Measurement, 211, 112603.
[19] Huang, M., Kuang, M., & Wu, R. (2024). 3D Reconstruction of Underground Cable Wells with Automatic Extraction of Point Cloud Contour Lines. Sensors & Materials, 36.
[20] Lin, S., Duan, L., Liu, J., Xiao, X., Miao, J., & Zhao, J. (2024). Automated geometric reconstruction and cable force inference for cable-net structures using 3D point clouds. Automation in Construction, 165, 105543.
[21] Yuan, Q., Chang, J., Luo, Y., Ma, T., & Wang, D. (2023). Automatic cables segmentation from a substation device based on 3D point cloud. Machine Vision and Applications, 34(1), 9.
[22] Han, X. F., Jin, J. S., Wang, M. J., & Jiang, W. (2018). Guided 3D point cloud filtering. Multimedia Tools and Applications, 77, 17397-17411.
[23] Zhang, F., Zhang, C., Yang, H., & Zhao, L. (2019). Point Cloud Denoising With Principal Component Analysis and a Novel Bilateral Filter. Traitement du signal, 36(5).
[24] Gou, F., Li, Y., Hou, C., & Wang, H. (2023). 3D point cloud global denoising algorithm based on different noise characteristics. Measurement Science and Technology, 35(1), 015032.
[25] Jia, C., Yang, T., Wang, C., Fan, B., & He, F. (2019). A new fast filtering algorithm for a 3D point cloud based on RGB-D information. PloS one, 14(8), e0220253.
[26] Cheng, D., Zhao, D., Zhang, J., Wei, C., & Tian, D. (2021). PCA-based denoising algorithm for outdoor lidar point cloud data. Sensors, 21(11), 3703.
[27] Dong, S., Jiao, Z., Zhou, L., Yan, Q., & Yuan, Q. (2023). A novel filtering method of 3D reconstruction point cloud from tomographic SAR. Remote Sensing, 15(12), 3076.
[28] Wang, X., Fan, X., & Zhao, D. (2022). PointFilterNet: A filtering network for point cloud denoising. IEEE Transactions on Circuits and Systems for Video Technology, 33(3), 1276-1290.
[29] Regaya, Y., Fadli, F., & Amira, A. (2021). Point-Denoise: Unsupervised outlier detection for 3D point clouds enhancement. Multimedia Tools and Applications, 80(18), 28161-28177.
[30] Zou, B., Qiu, H., & Lu, Y. (2020). Point cloud reduction and denoising based on optimized downsampling and bilateral filtering. Ieee Access, 8, 136316-136326.
[31] Li Wenguo,Luo Zixin,Hou Dameng & Mao Xueyi. (2021).Multi-line laser projection 3D measurement simulation system technology. Optik,231,